Commun Nonlinear Sci Numer Simulat 36 (2016) 192–203

Contents lists available at ScienceDirect

Commun Nonlinear Sci Numer Simulat

journal homepage: www.elsevier.com/locate/cnsns

Asymmetric counter propagation of domain walls

I. Andrade-Silva [a,*], M.G. Clerc [a], V. Odent [b]

[a] Departamento de Física, Facultad de Ciencias Físicas y Matemáticas, Universidad de Chile, Casilla 487-3, Santiago, Chile
[b] Université Lille, CNRS, UMR 8523 - PhLAM - Physique des Lasers Atomes et Molécules, Lille F-59000, France

ARTICLE INFO

Article history:
Received 28 September 2015
Revised 24 November 2015
Accepted 28 November 2015
Available online 7 December 2015

Keywords:
Liquid Crystals
Wave fronts
Nonlinear dynamics

ABSTRACT

Far from equilibrium systems show different states and domain walls between them. These walls, depending on the type of connected equilibria, exhibit a rich spatiotemporal dynamics. Here, we investigate the asymmetrical counter propagation of domain walls in an in-plane-switching cell filled with a nematic liquid crystal. Experimentally, we characterize the shape and speed of the domain walls. Based on the molecular orientation, we infer that the counter propagative walls have different elastic deformations. These deformations are responsible of the asymmetric counter propagating fronts. Theoretically, based on symmetry arguments, we propose a simple bistable model under the influence of a nonlinear gradient, which qualitatively describes the observed dynamics.

1. Introduction

Macroscopic systems influenced by injection and dissipation of energy and/or matter typically exhibit coexistence of different stable states– - this feature is usually denominated multistability [1–4]. Inhomogeneous initial conditions caused by inherent fluctuations generate spatial domains, which are separated by interfacial domain walls. These interfaces are known as front interfaces or domain walls [3,4]. Interfaces between these metastable states appear in the form of propagating fronts and give rise to a rich spatiotemporal dynamic [5–8]. Front dynamics have been observed in several contexts such as walls separating magnetic domains [9,10], directed solidification processes [11], nematic liquid crystals [12], oscillating chemical reactions [13], and fluidized granular media [14], among others. According to the dynamical system theory, in one spatial dimension, a front is a nonlinear solution that is identified in the co-moving frame system as a heteroclinic orbit linking two spatially extended uniform states [15]. The front type solutions can be regarded as a particle-type one, i.e., they can be characterized by a set of continuous parameters such as position, core width and so forth. The front propagation depends on the nature of the states that are being connected. For example, in the case of a front connecting a stable and an unstable state, its speed is not unique but determined by the initial conditions [16]. This scenario changes for a front connecting two stable uniform states. For variational or gradient systems, the most stable state invades the other one, in order to minimize its nonequilibrium energy or Lyapunov functional, in this sense, the front is always propagating towards the higher energy state [8]. There is only one point in the parameter space for which the front is motionless. Commonly called as Maxwell's point, it is the point for which both connected states have exactly the same energy [17]; close to this point, based on variational methods, one can analytically determine the front speed. Furthermore, far from the Maxwell's point, implicit expressions for the front speed can be obtained for variational systems [8], through the solution of the corresponding nonlinear eigenvalue problem.

* Corresponding author. Tel.: +56 988281459.
E-mail address: iandrade@ing.uchile.cl (I. Andrade-Silva).

http://dx.doi.org/10.1016/j.cnsns.2015.11.025
1007-5704/

In a bistable isotropic system, one expects that two counter-propagating fronts with the same speed can be created through a finite perturbation over the less favorable state, thus, making the most stable state to emerge. However, recently we have observed that perturbations of an Ising type walls in nematic liquid crystals with reflection symmetry generate two asymmetric counter-propagating fronts, each with a different speed and shape [18] [See Supplemental material for a movie that shows an example of asymmetric counter-propagating of domain walls in an inplane-switching cell filled with a nematic liquid crystal]. The perturbations are generated by the presence of glass spheres inside the liquid crystal sample. The dynamical behavior observed is common in systems under the influence of an external flow, i.e. drifting or convective systems [19]. In such case, the front that propagates in the drag force direction spreads faster than the one which propagates in the opposite direction. Likewise, the speed difference between the fronts accounts for the drag force. In addition, anisotropic propagation of point defect solutions with opposite topological charges has been reported in liquid crystals [20–22]. In this case the asymmetry of the propagation is due to the backflow around moving defects.

In this paper, we investigate in more detail the counter-propagation of asymmetrical domain walls connecting different molecular-orientation configurations in an in-plane-switching cell filled with a nematic liquid crystal without a flow, which we have recently observed [18]. These domain walls are triggered by the presence of glass bead within the sample. Experimentally, we characterize the profile and the speed of these fronts with respect to the amplitude and the frequency of the applied voltage to the liquid crystal cell. Based on the liquid crystal molecular orientation induced by the glass bead, we elucidate that the fronts generated by these spheres have different elastic deformations at the core of the fronts. These deformations are responsible for the asymmetry in the shape and speed of the fronts. Based on symmetry arguments, we propose a simple phenomenological equation – a bistable model under the influence of a nonlinear gradient – to describe the asymmetric counter-propagating fronts without flow. Analytically, we characterize the shape and the speed of the asymmetric counter-propagating fronts which qualitatively describes the observed dynamics. We evidence experimentally the kink formation due to the collision of two asymmetrical fronts and explain this phenomenon with a generalization of our simple phenomenological model.

2. Experimental front propagation

2.1. Experimental setup

To investigate the propagation of domain walls, we have considered an in-plane-switching cell filled with a nematic liquid crystal. The experimental setup under study is depicted on Fig. 1. A layer of *E*7 nematic liquid crystal is inserted between two glass plates, thickness $g = 1$ mm, with a cell gap $d = 8.8 \pm 0.2\,\mu$ m. The elastic constants of the liquid crystal under consideration are, respectively, $K_1 = 11.2$, $K_2 = 6.8$, and $K_3 = 18.6$ ($\times 10^{-12} N$). The parallel and the perpendicular dielectric constants are $\varepsilon_{\parallel} = 18.96$ and $\varepsilon_{\perp} = 5.16$ [23–26]. We consider an in-plane-switching cell, with a homogeneous planar alignment (following *y*-axis, cf. Fig. 1) and a perpendicular rubbing to the electric field (Instec, *IPS*02*A*88*uX*00). The indium tin oxide (ITO) electrode width and the gap width are the same, $e = 15\,\mu$ m. The height of the electrodes is negligible (∼25 nm) compared to the cell thickness ($d = 8.8\,\mu$ m). The active zone is a square of side $l = 1$ cm. Under these settings, we can consider the cell in a good approximation as an infinite thin film medium. The electrodes are aligned in the direction of *y*-axis, that is, the molecules are anchored parallel to the electrodes (see Fig. 1). The electrodes are connected to a function generator, applying an alternating current voltage with frequencies ∼1 Hz–10 MHz and an amplitude ∼0 Vpp–20 Vpp (Volt peak-to-peak). The cell is illuminated with a white light placed between a polarizer *P* and an analyzer *A*. In order to have a better information about the molecular orientation the polarizers can be placed parallel (//) or perpendicular ($\perp$) related to each other. The microscope magnification used is 20 × or 50 × . The liquid crystal dynamics is measured and recorded through a charge couple device camera (CCD) connected to an optical microscope.

2.2. Experimental observation of asymmetrical counter propagative fronts

We consider the system under study as an infinite liquid crystal medium. A good approximation of this, is to observe in the middle of the sample a small portion of the cell. This midplane is schematically depicted in Fig. 3d. By direct observation, without applying a voltage to the sample, only the electrode bands can be detected. Fig. 3a and top panel in Fig. 2a show these electrode bands characterized by dark zones. Note that there is a black bead between two consecutive electrodes. This bead is a glass sphere used to fix the thickness between the two glass plates, with diameter of 8.8 μ m. The glass sphere creates a 3D local perturbation in the molecules orientation around it. Applying a voltage with an amplitude of 20 Vpp and a frequency of $f = 1$ kHz, the system exhibits two asymmetric domain walls propagating towards both sides from the glass sphere, following *y*-axis (cf. Fig. 2). These fronts connect two different molecular orientations, which correspond to black bands observed over the electrodes and between them. Figs. 2 and 4 illustrate the front profiles. To demonstrate the constancy of front velocity, we represent on Fig. 2 dotted lines, blue for the left front and green for the right one, which match with the front positions for every snapshot. We note that each front propagates with constant speed, however, different between each other.

The black curves are the consequence of the molecular orientations in the sample which modify the light polarization and do not allow the light to cross the analyzer. As a result of the electrode shapes, the states that connect the fronts are not uniforms in the vertical direction. Between the gap and the middle electrode, the system exhibits three equilibria, represented by α, β and γ in Fig. 4a, and observed thanks to the use of crossed polarizers. The fronts only connect two particular molecular orientations. One is positioned in the center of the gap region (α-state, see Figs. 3c and 4 a) and the other one close to the center of the electrode

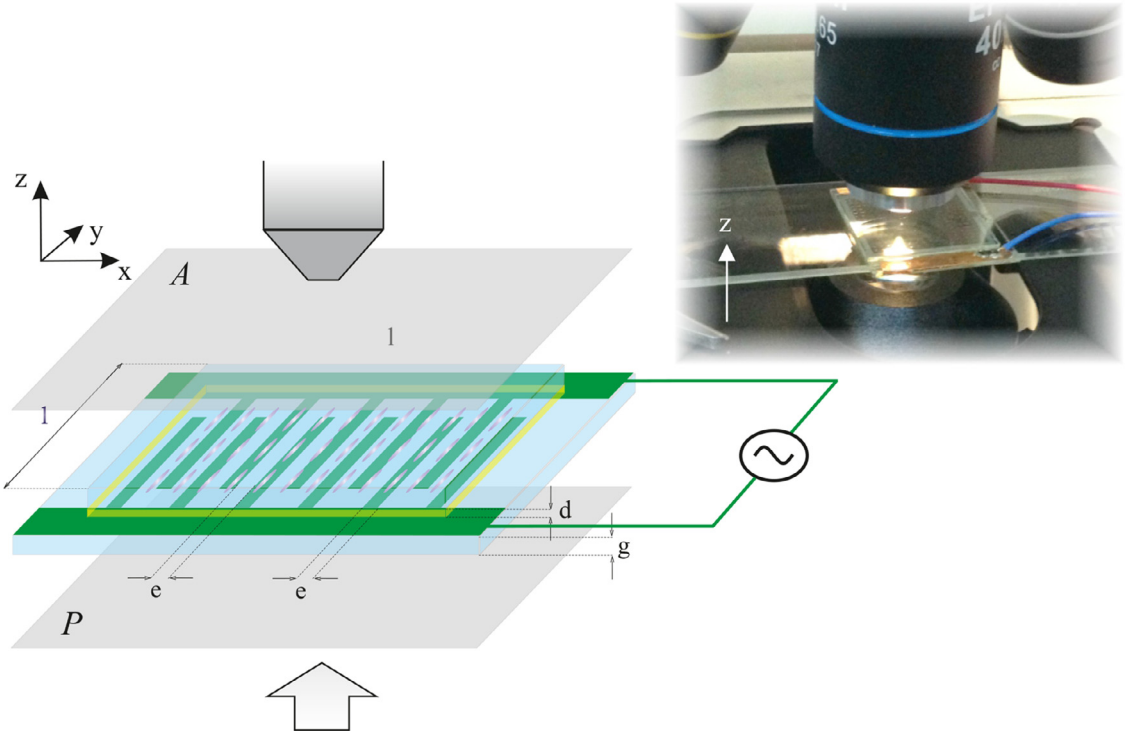

Fig. 1. Sketch of the experimental setup, which represents an in-plane-switching cell connected to a generator and observed by a microscope (top), with a 40X magnification, in white light (down). Thickness between the two glass plates, $d = 8.8 \pm 0.2\,\mu$ m. Thickness of a glass plate, $g = 1$ mm. Active zone, $l \times l = 1\,\text{cm}^2$. Gap between two electrodes, $e = 15\,\mu$ m. Perpendicular polarizer to the molecules anchoring, $P_\perp$ (following x-axis). Parallel polarizer to the molecules anchoring, $P_\parallel$ (following y-axis). The inset shows a snapshot of the experimental system under study. (For interpretation of the references to color in this figure legend, the reader is referred to the web version of this article.)

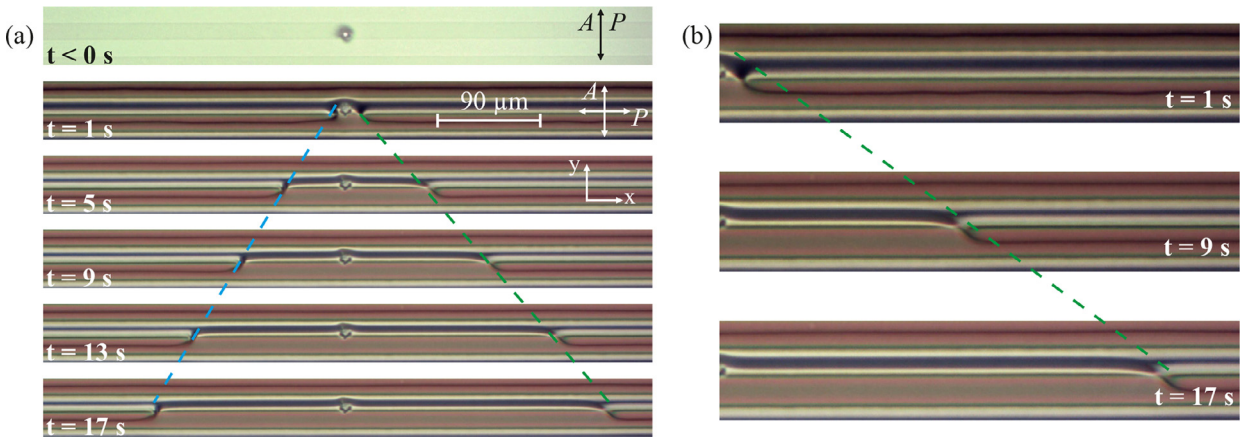

Fig. 2. Asymmetric counter propagating domain walls in an in-plane-switching cell filled with an *E*7 nematic liquid crystal, applying a tension of $T = 20$ V and $f = 1$ kHz. (a) Experimental snapshots at different times. The black disk in the center is a glass sphere and the dashed lines emphasize the speed with which fronts propagate. (b) Amplified snapshots of the right front. (For interpretation of the references to color in this figure legend, the reader is referred to the web version of this article.)

(β-state). Notice that at the center of the electrodes, the system presents a peculiar molecular orientation γ-state. These states account for molecules orientation with a certain preferential vertical and horizontal direction, as illustrate in Fig. 3d. The most stable molecular orientation (β-state) invades the least favorable one (α-state, cf. Fig. 4). Indeed, the states over the electrodes are more stable than those between them.

As we have mentioned, in a bistable isotropic system, one expects a finite disturbance on a less favorable state can generates two counter propagative fronts with the same speed, giving appearance of the most stable one. Notwithstanding, we have

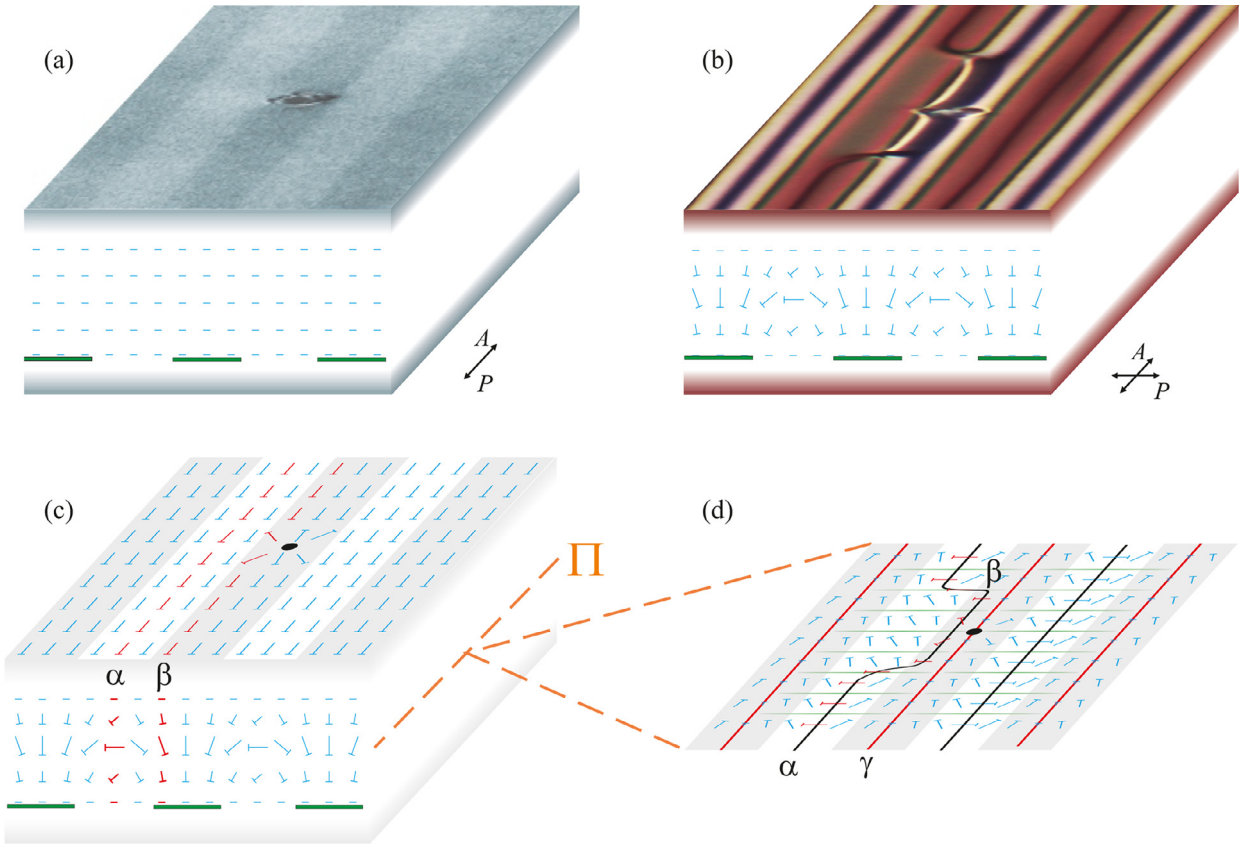

Fig. 3. Schematic representation of the liquid crystal layer. Experimental image on the top of the sample, (a) without voltage and parallel linear polarizers and (b) with voltage, observed between crossed polarizers. Schematic molecules orientation in the liquid crystal sample (c) without voltage. (d) Schematic molecular representation in the middle plane of the sample, Π, with voltage. Glass ball causing a local perturbation and $\{\alpha, \beta, \gamma\}$ stand for different domain walls. (For interpretation of the references to color in this figure legend, the reader is referred to the web version of this article.)

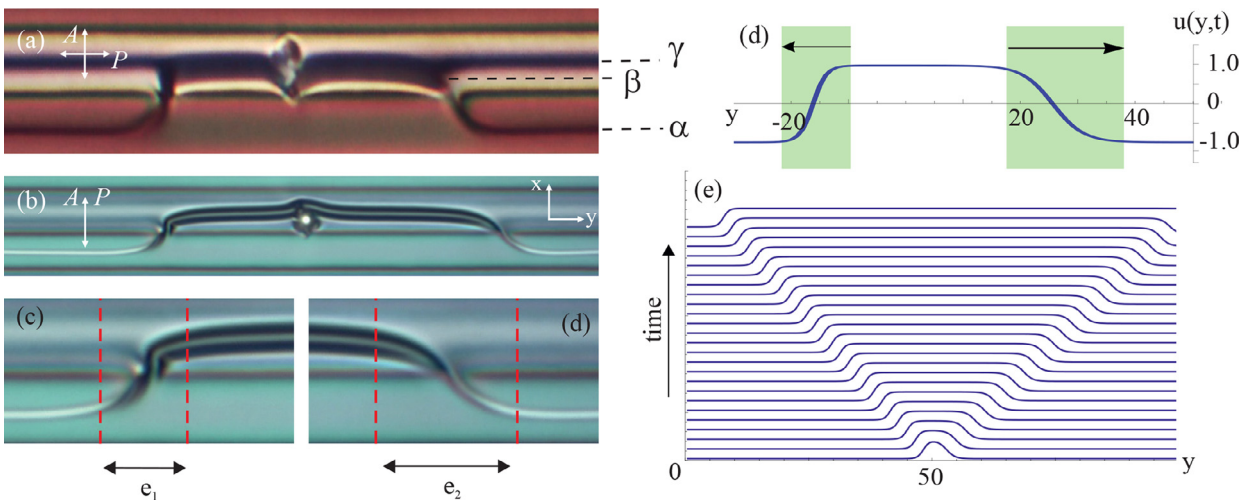

Fig. 4. Front profiles. (a) Experimental counter propagative fronts connecting two different molecular orientation, from Fig. 1, at $t = 10$ s with cross linear polarizers. (b) Experimental counter propagative fronts under parallel linear polarizers. (c) Left front with a core size e_1. (d) Right front with a core size e_2. (d) Stationary solution of bistable model Eq. (1) for $\eta = 0$ and $\nu > 0$. (e) Spatiotemporal diagram of counter propagative fronts of the model Eq. (8) for $\eta = 0.3$ and $\nu = 0.6$. (For interpretation of the references to color in this figure legend, the reader is referred to the web version of this article.)

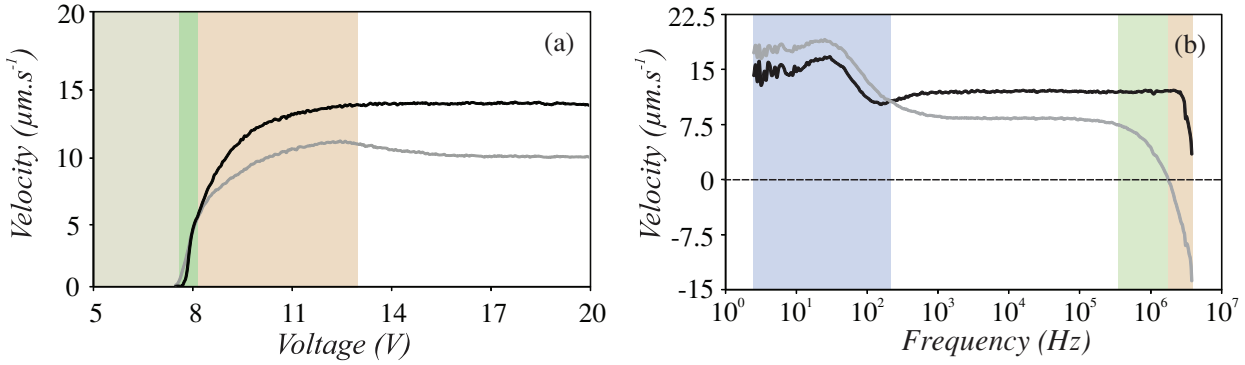

Fig. 5. Experimental characterization of front velocities. (a) Velocities versus voltage amplitude with a fix frequency value, $f = 1$ kHz, and (b) velocities versus frequency with a fix amplitude value $V_0 = 20$ Vpp. The black and the grey curves are, respectively, the speed of right and left front. The black and gray curves account for the right and the left front speed, respectively, using Fig. 2 as a reference orientation.

observed that perturbations of an Ising type walls in nematic liquid crystals with reflection symmetry generate two asymmetric counter propagative fronts (see Fig. 2). Indeed, the speed and the shape of each front are different. It is worthy to note that the perturbations are generated by the presence of glass spheres inside the liquid crystal sample. In the other hand, asymmetric front propagation is typically observed in drifting or convective systems , that are systems under the influence of a flow. The presence of the drift force causes the reflection symmetry breaking, where the front that propagates in the direction of the drag force spreads faster than the one which propagates in the opposite direction. Likewise, the speed difference between the fronts accounts for the drag force.

The origin of the observed asymmetry between the front is: each core separates different molecular orientations, whereby in the left front the directors rotate clockwise and in the right front they rotate counterclockwise [cf. Fig. 3d]. Therefore, as a result of the anisotropic properties of the nematic liquid crystal (i.e., elastic constants [23–26]), the unlike front cores have molecular configurations with different twisting energy. Moreover, it is also expected that the director rotation is coupled with the velocity field to generate an asymmetric backflow [23–26]. These effects are responsible for the dissimilar propagation speeds.

2.3. Velocity evolution

The two fronts present constant velocities during their propagation in the sample. It is possible to change the front velocity values by modifying the voltage parameters. Fig. 5 shows the front speeds versus the voltage amplitude for a fix value of the frequency, $f = 1$ kHz, on the left panel and the frequency for a fix value of the voltage amplitude voltage, $V_0 = 20$ Vpp, on the right panel. The black and gray curves account for the right and the front speed, using Fig. 2 as a reference orientation. Concerning the voltage amplitude, we observed qualitatively four different regimes. In the region of low voltage, corresponding at $V_0 \lesssim$ 7.5 Vpp, the tension is not enough to induce the molecular reorientations, i.e. the system does not exhibit other orientations than those induced by the anchoring conditions. Hence, in this region we do not observe fronts. For $V_0 \simeq 7.5$ Vpp (region II), we have observed the emergence of domain walls. Therefore, this voltage corresponds to the critical value which accounts for the Freederickz transition [23–26]. Each front separates different molecular orientation states. The counter-propagative fronts spread with almost the same speed ($v_{front} \sim 5\,\mu$m/s). The left front is slightly faster than the right one. In region III, between $V_0 \simeq 9$ Vpp and $V_0 \simeq 12.5$ Vpp, we observe a significant increment of the front speed values. The right front propagates faster than the left one. In the region IV, for $V_0 \gtrsim 12.5$Vpp, the system exhibits a stationary behavior for counter-propagative fronts. The right and left front speed are constant v_{front}(right) $\approx 13.5\ \mu$m/s and v_{front}(left) $\approx 9.5\ \mu$m/s).

The situation looks a little bite more complex, when we modify the voltage frequency inside the cell. For lower frequency than 3 Hz, the molecules oscillate with large amplitude, and then, there are no privileged stable molecular orientations. For frequencies in the range [3, 200]Hz, the speed of domain walls exhibit a resonant phenomenon, that is, the speed of domain walls has a maximum at a given frequency (cf. Fig. 5b). This maximum speed is reached at around 30Hz. In this range, the right front propagates faster than the left one. At frequency $f = 210$Hz, the two counter propagating fronts have the same speed. Above this value the two speeds do not present substantive modification until 1 MHz. From $f = 1$ MHz, the two front velocities present a strong and fast modification (in log-scale). The right front speed decrease until v_{front}(right) $\approx 3.5\ \mu$ m/s for $f = 3.8$ MHz. The left front speed also decreases. At $f = 1.8$ MHz, the left front propagates in the same direction of the right one and changes consequently its velocity sign. At $f = 3.9$ MHz the two fronts disappear.

From the above description, we can conclude that it exists an optimal parameter range to observe a constant dynamics of asymmetrical counter propagative fronts for voltages $V_0 \epsilon$ [14; 20]Vpp and frequencies $f \epsilon$ [1; 100]kHz.

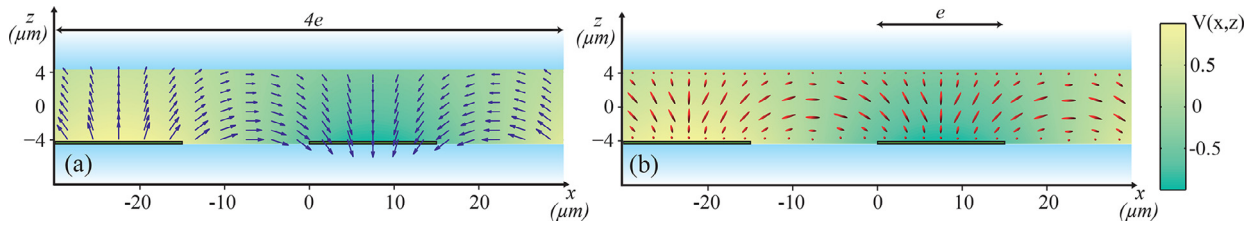

Fig. 6. (a) Electric field representation inside the liquid crystal sample using formulas (2) and (3). (b) The molecular orientation in the liquid crystal sample. The electric potential is represented by the gradient colors. (For interpretation of the references to color in this figure legend, the reader is referred to the web version of this article.)

3. Theoretical description of the asymmetrical counter propagative fronts

3.1. Voltage and electric field inside the nematic liquid crystal cell

The in-plane-switching technology, as presented in Section 2.1, is composed by two electrode combs nested all in all and deposed on a glass layer inside the liquid crystal cell, as depicted on the experimental setup on Fig. 1. This electrode configuration generates an inhomogeneous periodic electric field [28]. To characterize this type of cells, we develop a model of the electric field inside the sample. The nematic liquid crystal is an anisotropic medium, so the voltage $V(x, y, z)$ inside the cell satisfies an anisotropic Laplace equation, which has the form

$$\partial_{xx}V + \frac{\epsilon_{\parallel}}{\epsilon_{\perp}}\partial_{yy}V + \partial_{zz}V = 0,$$

where $\epsilon_{\perp}$ and $\epsilon_{\parallel}$ are, respectively, the perpendicular and the parallel dielectric constants to the nematic director. The dielectric anisotropy is defined as $\epsilon_a \equiv \epsilon_{\parallel} - \epsilon_{\perp}$ and it is positive for the liquid crystal used in our experiment, $\epsilon_a > 0$. At the bottom glass, the voltage satisfies the boundary condition $V(x, y, -d/2) = f(x)$, with $f(x)$ a periodical function which follows the electrodes periodicity, i.e. $f(x + 4e) = f(x)$ where e is the electrode size and $4e$ is the wavelength. Assuming that the liquid crystal and the glass have similar dielectric constants, then no boundary effects are considered at the top layer and we use the condition $V(x, y, z = +\infty) = \tilde{0}$. Alternatively, one can consider that the voltage is constant in the top glass, $V(x, y, z = d/2) = V'$, qualitatively similar results as been obtained into an in-plane-switching liquid crystal cell, for instance see Ref. [27].

Using the Fourier transform in x-coordinate, neglecting the dependence on the y-coordinate and solving the anisotropic Laplace equation with the corresponding boundary conditions, after straightforward calculations one obtains

$$V(x, z) = \frac{1}{2\pi}\int dk dx' f(x') \exp\left[-ik(x' - x) - k\left(z + \frac{d}{2}\right)\right]. \tag{1}$$

For the sake of simplicity, we consider $f(x) = V_0 \cos(k_0 x)$, with $k_0 \equiv \pi/2e$. Thus the voltage inside the cell takes the form

$$V(x, z) = V_0 \cos(k_0 x) e^{-k_0(z+d/2)}, \tag{2}$$

then the voltage is a periodical function in the transverse direction and a decreasing function in the vertical direction. The electric field $\mathbf{E} = -\nabla V$ inside the sample has the explicit form

$$\mathbf{E} = V_0 k_0 \sin(k_0 x) e^{-k_0(z+d/2)}\hat{x} + V_0 k_0 \cos(k_0 x) e^{-k_0(z+d/2)}\hat{z}. \tag{3}$$

Fig. 6a depicts the electric potential and the electric field in the liquid crystal sample from formulas (2) and (3). Since the liquid crystal has positive anisotropic constant ϵ_a, the molecules align with the electric field. Fig. 6b shows the expected equilibrium structure for a director within the liquid crystal sample. Then the electric field induces naturally nematic Ising walls along the electrodes. This electric field configuration also induces domain walls between the electrodes. Under the microscope, we observed that the edges of the electrodes also induce domain wall. Notice that these domain walls are complicated because they are inhomogeneous, then, a description from first principles is a complex task. Our strategy to describe the dynamics of domain walls was based on symmetry arguments.

3.2. Nematic asymmetrical fronts

The interface between two states in a thin film layer corresponds to a curve. Hence, it can be treated as a one-dimensional system describing the temporal evolution of the local wall position $u(y, t)$, where y parameterizes the interface. We observe that the wall position has two equilibria (states α and β in Fig. 3) corresponding to different molecular configurations states and the system exhibits fronts connecting these two states. A simple bistable model which exhibits fronts reads

$$\partial_t u = \eta + u - u^3 + \partial_{yy}u, \tag{4}$$

where η is a parameter that measures the relative stability among both equilibria. These equilibria are energetically equivalent for $\eta = 0$. This bistable model has reflection symmetry ($y \to -y$) and is variational, or gradient, which means that can be rewritten

as follows

$$\partial_t u = -\frac{\delta F}{\delta u}, \tag{5}$$

where

$$F = \int dy \left\{ -\eta u - \frac{u^2}{2} + \frac{u^4}{4} + \frac{(\partial_y u)^2}{2} \right\} \tag{6}$$

is the Lyapunov functional. Hence, the system evolves by the minimization of the Lyapunov functional. Likewise, this system has an unstable homogeneous state and two stable ones provided for $|\eta| < 2/(3\sqrt{3})$. For small η the unstable and stable equilibria are $u \simeq 0$ and $u_\pm \simeq \pm 1$, respectively. In bifurcation theory, the model Eq. (4) describes an extended imperfect Pitchfork bifurcation [3,4]. At the Maxwell Point, $\eta = 0$, both equilibria are energetically equivalent and the system has motionless front type solutions of the form

$$u_{\leftrightarrows}(y) \equiv \pm \tanh\left[\frac{(y - y_0)}{\sqrt{2}}\right], \tag{7}$$

which connect asymptotically the states $u = 1$ and $u = -1$. The parameter y_0 denotes the front position and parameterizes the family of front solutions as result of translation symmetry. When $\eta \neq 0$, there is an energy difference between the states and the system exhibits propagating fronts, which move at a constant speed invading the less stable state. Indeed, one observes that two counter-propagating fronts with the same speed can be created through a finite perturbation over the less favorable state, thus, making the most stable state to emerge. Therefore, the model Eq. (4) does not account for the observed dynamics in the liquid crystal cell with in-plane-switching.

To model asymmetric counter propagating one-dimensional fronts, let us introduce the following phenomenological bistable model under the influence of a nonlinear gradient

$$\partial_t u = \eta + u - u^3 + \partial_{yy} u + \nu u \partial_y u, \tag{8}$$

where $u(y, t)$ is an order parameter that accounts for the position of the domain wall separating the different molecular configurations and $\{\eta, \nu\}$ are parameters that respectively control the relative stability of the equilibria and the asymmetry of the system. The last term is a non-variational type and corresponds to a Burgers drift that breaks the symmetry $y \to -y$. This term accounts for the asymmetric elastic deformations induced to connect the different molecular configurations (see Fig. 3). For $\nu = 0$, we recover the previous model Eq. (4) with symmetric front type solutions. Solutions to this model for $\eta = 0$ were studied [29] and used after to describe fixed-flux convection in a tilted slot [30]. Note that changing the sign of ν is equivalent to doing the transformation $y \to -y$, so we set $\nu > 0$ without loss of generality. For $\eta = 0$, this model has an unstable homogeneous state $u = 0$ and two stable homogeneous ones, $u_\pm = \pm 1$. Moreover, this model has motionless fronts of the form

$$u_{\leftrightarrows}(y) \equiv \pm \tanh\left[\frac{(y - y_0)}{c_{\leftrightarrows}}\right], \text{ with } \; c_{\leftrightarrows} > 0. \tag{9}$$

The solution $u_{\leftarrow}(y, y_0)$ $[u_{\rightarrow}(y, y_0)]$ represents a front connecting the states u_- $[u_+]$ with u_+ $[u_-]$ when the y-coordinate is incremented. We name these solutions as *left front* and *right front*, respectively. The parameter y_0 denotes the front position. Note that the core sizes are $c_{\leftrightarrows}$. In order to take into account the effect of the Burgers drift, using the motionless front as ansatz (9) in Eq. (8) after straightforward calculations we obtain

$$c_{\leftrightarrows} = \mp\frac{\nu}{2} + \sqrt{\left(\frac{\nu}{2}\right)^2 + 2}.$$

When $\nu = 0$, we recover the motionless front formula (7). Notice that $c_{\leftarrow} < c_{\rightarrow}$. Hence, the left front core is thinner than the right front one. Figs. 4d and e show these fronts, which present a qualitative agreement with the experimentally observed fronts. Fig. 7 shows a profile comparison between the observed fronts and formula (9). Indeed, these figures show that there is a good agreement between the experimental and the analytical profile fronts using the bistable model. All numerical simulations presented in this work were conducted using Runge–Kutta order 4 algorithm and finite elements method.

When one considers that the asymptotic equilibria have different energies, $\eta > 0$ ($\eta < 0$), the asymmetric fronts move at different constant asymptotic speeds, such that the most favorable state, u_+ (u_-), invades the less favorable one u_- (u_+). To get analytically the front speed, we consider that $\{\eta, \nu\}$ are small enough and use the ansatz $u(x, t) = u_{\leftrightarrows}[y - y_0^{\leftrightarrows}(t)] + w(y, t)$, where the front position $y_0^{\leftrightarrows}(t)$ is promoted to a temporal function and $w(y, t)$ stands for a small correction of order $\{\eta, \nu\}$. Introducing the above ansatz in Eq. (8), linearizing in w and neglecting the terms $\dot{w}$, $\nu u_{\leftrightarrows} \partial_y w$, and $\nu(\partial_y u_{\leftrightarrows}) w$, we obtain

$$\left(1 - 3(u_{\leftrightarrows})^2 + \partial_{yy}\right) w = -\partial_y u_{\leftrightarrows} \frac{dy_0^{\leftrightarrows}}{dt} - \eta \tag{10}$$

In the left hand side of Eq. (10) we can use the following approximation

$$u_{\leftrightarrows} \approx u_{\leftrightarrows}^{(0)} \equiv u_{\leftrightarrows}|_{\nu=0} = \pm \tanh\left(\frac{(y - y_0)}{\sqrt{2}}\right).$$

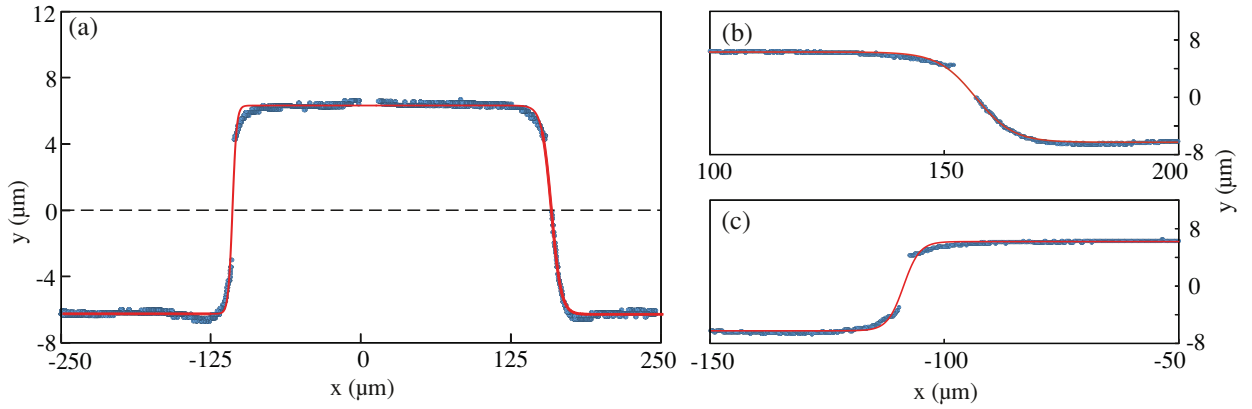

Fig. 7. Experimental versus theoretical front profiles. Points are obtained from the experimental domain walls. (a) Asymmetrical counter propagation of fronts. The solid curve is obtained using the fitting formula $u(y) = r_0[\tanh((y+396.5)/c_{\leftarrow}) - \tanh((y-131)/c_{\rightarrow}) - 1]$ with $c_{\rightarrow} = 7.98$, $c_{\leftarrow} = 3.43$, and $r_0 = 6.275$; (b) right front, the continuous curve is obtained using the formula $u_{\rightarrow}(y) = -r_0[\tanh((y-131)/c_{\rightarrow})]$; (c) Left front, the continuous curve is obtained using the formula $u_{\leftarrow}(y) = r_0[\tanh((y+396.5)/c_{\leftarrow}]$ (For interpretation of the references to color in this figure legend, the reader is referred to the web version of this article.).

So, Eq. (10) has the form $\mathcal{L}w = b$ with

$$b = -\eta - \partial_y u_{\leftrightarrows}^{(0)} \frac{dy_0^{\leftrightarrows}}{dt},$$

and

$$\mathcal{L} = \left(1 - 3(u_{\leftrightarrows}^{(0)})^2 + \partial_{yy}\right).$$

$\mathcal{L}$ is an Hermitian operator in respect to the inner product $\langle f|g\rangle \equiv \int_{-\infty}^{+\infty} fg\,dy$ and has a Goldstone mode as consequence of the translation invariant given by $\mathcal{L}\left(\partial_y u_{\leftarrow}^{(0)}\right) = 0$. To solve the linear equation $\mathcal{L}w = b$, we impose *Fredholm alternative*, that is, the right-hand side orthogonal to the kernel of $\mathcal{L}^{\dagger}$ [3,31]. This alternative leads to the following equation $\langle \partial_y u_{\leftarrow}^{(0)}|b\rangle = 0$. Thus, the *left* and *right front* speeds are given by

$$\frac{dy_0^{\leftrightarrows}}{dt} = -\eta \frac{\left\langle \partial_y u_{\leftarrow}^{(0)}|1\right\rangle}{\left\langle \partial_y u_{\leftarrow}^{(0)}|\partial_y u_{\leftrightarrows}\right\rangle}. \tag{11}$$

The integral in the numerator gives $\left\langle \partial_y u_{\leftarrow}^{(0)}|1\right\rangle = 2$. To perform the integral in the denominator we need to expand the term

$$\partial_y u_{\leftrightarrows} \simeq \partial_y u_{\leftrightarrows}^{(0)} + \nu \partial_\nu \left(\partial_y u_{\leftrightarrows}\right)\big|_{\nu=0},$$

where

$$\partial_\nu \left(\partial_y u_{\leftrightarrows}\right)\big|_{\nu=0} = \pm\partial_\nu \left(\frac{1}{c_{\leftrightarrows}} \operatorname{sech}^2\left(\frac{y-y_0}{c_{\leftrightarrows}}\right)\right)\Bigg|_{\nu=0} = \frac{1}{4}\operatorname{sech}^2\left(\frac{y-y_0}{\sqrt{2}}\right) - \frac{1}{2}\operatorname{sech}^2\left(\frac{y-y_0}{\sqrt{2}}\right)\tanh\left(\frac{y-y_0}{\sqrt{2}}\right)\left(\frac{y-y_0}{\sqrt{2}}\right).$$

Performing the integrals and after straightforward calculations, we obtain at dominate order

$$\left\langle \partial_y u_{\leftarrow}^{(0)}|\partial_y u_{\leftrightarrows}\right\rangle \approx \pm\frac{2\sqrt{2}}{3} + \frac{1}{6}\nu. \tag{12}$$

From Eq. (11), the left and the right front speeds are given by

$$\frac{dy_0^{\leftrightarrows}}{dt} \simeq \mp\frac{3}{\sqrt{2}}\eta + \frac{3}{8}\eta\nu. \tag{13}$$

The first term on the right hand side accounts for the energy difference between both equilibria. The last term accounts for the effect of Burgers drift, which clearly follows that the right front (left front) is faster than the left front (right front) for $\eta > 0$ ($\eta < 0$). Hence, the front with wider core is always fastest. In order to validate the above analytical expressions in comparison with numerical simulations of Eq. (8), we introduce the following parameters

$$V_{var} \equiv \frac{\left(\dot{y}_0^{\rightarrow} - \dot{y}_0^{\leftarrow}\right)}{2} \simeq \frac{3}{\sqrt{2}}\eta, \tag{14}$$

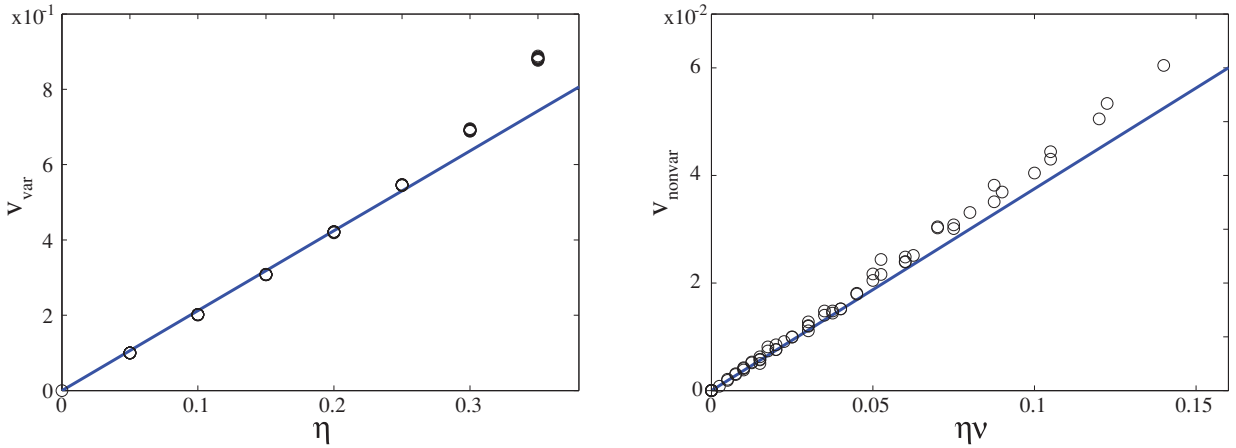

Fig. 8. Numerical measurements of the parameters V_{var} and V_{nonvar} for different values of η and ν. The points are obtained from directed numerical simulation of model Eq. (8) and the continuous lines are obtained used the analytical formulas (14) and (15), respectively. (For interpretation of the references to color in this figure legend, the reader is referred to the web version of this article.)

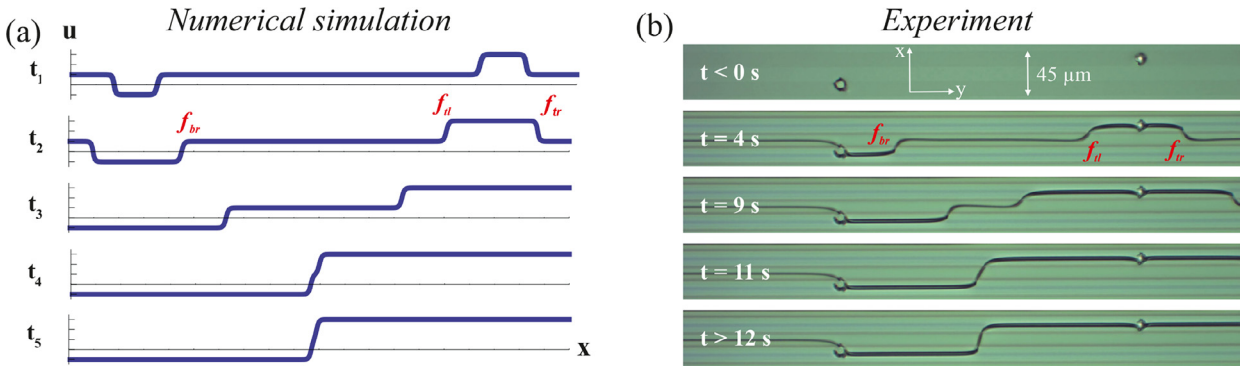

Fig. 9. Numerical and experimental observations of front propagation between different molecular reorientations and kink formation between two symmetrical molecular orientation. (a) Temporal sequence of numerical profiles of model Eq. (16) with $\eta = 0.2$, $\nu = 0.5$ and $t_1 < t_2 < t_3 < t_4 < t_5$. b) Sequence of snapshots of asymmetric counter propagating domain walls in an in-plane-switching cell filled with an $E7$ nematic liquid crystal under parallel polarizers, applying a tension of $T = 20$Vpp and $f = 1$ kHz. (For interpretation of the references to color in this figure legend, the reader is referred to the web version of this article.)

and

$$V_{nonvar} \equiv \frac{\left(\dot{y}_0^{\rightarrow} + \dot{y}_0^{\leftarrow}\right)}{2} \simeq \frac{3}{8}\eta\nu. \tag{15}$$

The parameter V_{var} stands for the front speed due to the difference in energy between both states, i.e., this is the speed of variational origin. Additionally, the parameter V_{nonvar} accounts for the front speed originated by the non-variational drift. Note that

$$\frac{dy_0^{\leftrightarrows}}{dt} = \pm V_{var} + V_{nonvar}.$$

Numerical measurements of V_{var} and V_{nonvar} are depicted in Fig. 8 showing a quite good agreement with our analytical findings. It is important to note that the formulas for the speed (14) and (15) are only valid for $\{\nu, \eta\}$ small.

4. Kink formation

Because of the periodicity of the electrodes, one expects that the system exhibits many domain walls and has the possibility to connect states from different electrodes (see Fig. 9).

4.1. Theoretical explanation of kink formation

To take into account the periodicity of the wall lattice, we propose a generalization of the bistable model (8) (periodic multistable model)

$$\partial_t u = \sin(\pi u) - \eta \cos\left(\frac{\pi u}{2}\right) + \partial_{yy} u + \nu \sin(\pi u)\partial_y u, \tag{16}$$

which can be rewritten in the following form

$$\partial_t u = -\frac{\partial V}{\partial u} + \partial_{yy} u + \nu \sin(\pi u)\partial_y u, \tag{17}$$

where

$$V(u) = \frac{\cos(\pi u)}{\pi} + \frac{2\eta}{\pi} \sin\left(\frac{\pi u}{2}\right). \tag{18}$$

For $\eta = 0$, the stable equilibria are given by $u_n = 2n + 1$ with $n = \{\pm 1, \pm 2, \ldots\}$. The Burgers drift term has been modified to be consistent with the periodicity of $u(y, t)$. This model can exhibit fronts connecting the state $u_n = 2n + 1$ with the top state ($u_{n+1} = 2n + 3$) or the bottom state ($u_{n-1} = 2n - 1$). The front connecting a middle state with a top one and propagate to the right (left) is denoted by f_{tr} (f_{tl}). Analogously, if the front connects a bottom state, we use the notation $\{f_{bl}, f_{br}\}$. The parameter η controls the relative stability between the even states and the odd states. Between two consecutive equilibrium states, this model has qualitatively the same dynamic behavior exhibited by bistable model Eq. (8). However, as a result of multiple stability, this system can have a richer domain walls dynamic. In particular, this model exhibits kink formation when two opposite fronts connecting different states collide. A kink wall corresponds in general to a motionless front connecting two symmetric states. Two counter propagative fronts connecting monotonously a bottom-middle-top state have equal speeds in opposite direction giving result to a stationary kink. Fig. 9 illustrates the experimental and numerical kink formation showing a similar behavior.

4.2. Experimental kink formation

We expect to observe experimentally the kink formation in our sample, as predicted by our theoretical model (Section 4), between two identical molecular deformations. We search in our sample, a place where there are two or more glass beads located on two electrodes, separated by only one gap, as presented in Fig. 9b at $t < 0$ s. We need to have a front between the top electrode and the central gap, created by the top glass bead and another front between the bottom electrode and the central gap, generated by the bottom glass bead (Fig. 9a at $t = 4$s). When we apply a voltage, we observe on the top two counter propagating fronts f_{tl} and f_{tr}, whereas on the bottom only one propagating front to the right f_{br}. [See Supplemental material for a movie that shows kink formation]. This configuration is enough to observe the kink formation. During 11 s, f_{tl} and f_{br} propagate towards each other. At $t = 11$ s, The two fronts collide each other to form a kink wall, which connects the two electrodes. We observe a

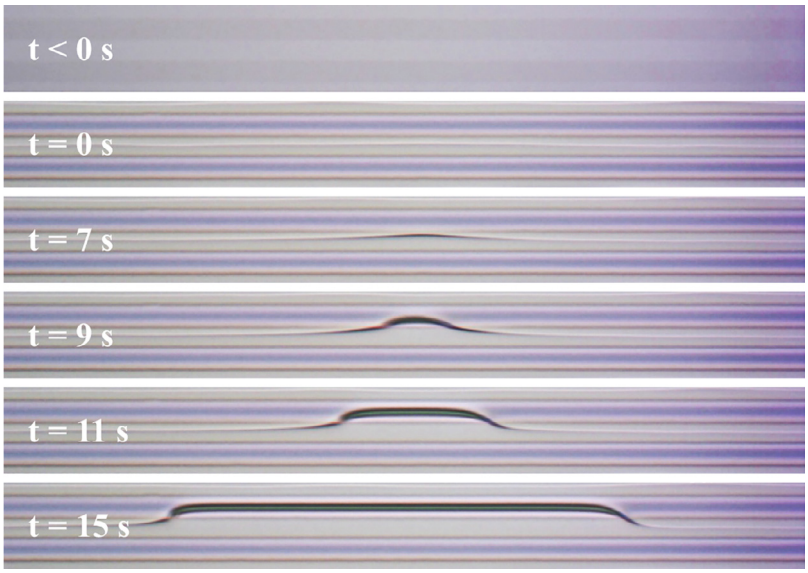

Fig. 10. Experimental observation of asymmetrical front propagation without local perturbation (glass sphere). Temporal sequence of snapshots with a tension of the for $V = T_0 + T\sin(ft)$, $T = 16$Vpp, $T_0 = 2$V, and $f = 1$kHz. (For interpretation of the references to color in this figure legend, the reader is referred to the web version of this article.)

steepness changing between $t = 11$ s and $t > 12$ s. This effect comes from the velocity difference between the fronts and the kink. At $t = 11$ s, the two front have just collapsed and the smooth steepness is due to the front velocity. Contrary to $t > 12$ s, where the kink is established and motionless, in this case the steepness is more important.

5. Front formation without local perturbation

Experimentally, it is possible to observe counter propagative fronts without glass sphere to generate the local perturbation. By adding an input offset to the alternative component of the voltage Eq. (2), as $V(x, y, z) + V_1$, with $V_1 < V(x, y, z)$, we observe the destabilization of the molecular orientation between two electrodes (see Fig. 10). We explain this phenomenon by the presence of some inhomogeneities in the media, which, combined with the offset, change locally the molecular stability and generate the front propagation. If, we increase more V_1, only the β state (cf. Fig. 3) exists and the black line of the α state disappears. In other words, we change globally and not locally, the molecular orientation stability.

6. Conclusion

In conclusion, we have studied counterpropagation of asymmetrical fronts connecting different molecular orientations in an in-plane switching cell filled with nematic liquid crystal without flow. These fronts connect two equilibrium positions of the walls generated over the electrodes of the cell. Experimentally, we have characterized the profile and the speed of theses fronts. Two counterpropagating fronts had different elastic deformation at their cores. These deformation are responsible for the asymmetry in the shape and the speed of the fronts. Theoretically, we have proposed a phenomenological equation, a bistable model under the influence of a nonlinear gradient, to describe asymmetric counterpropagating fronts without flow. Analytically, we have derived the shape and speed of the fronts exhibited by the model in the limit of small asymmetry between equilibria. We have quite good agreement with numerical simulations. We have generalized this model to emphasizes the periodicity of the cell and predicted stationary kink formed when fronts from two electrodes collide. The analytical results from the models describe qualitatively the observed dynamics in a large range of parameters. It is worthy to note that, the system exhibits qualitative changes in the behavior of front propagation for large and small frequencies. For low frequencies fronts exhibits a resonance phenomenon for speed and for high frequency the system displays inversion of propagation of one of the fronts. The study and understanding of these phenomena is in progress.

Acknowledgments

The authors thank F. Roussel and C. Binet for their fruitful discussions and N. Maalouli for the critical reading of the manuscript. M. G. C. thanks for the financial support of FONDECYT projects 1150507. V.O. acknowledges the support of the 'Région Nord- Pas-de-Calais'. This work has been partially supported by the Centre National de la Recherche Scientifique (CNRS), the Ministry of Higher Education and Research, the Nord-Pas de Calais Regional Council and European Regional Development Fund (ERDF) through the Contrat de Projets Etat-Région (CPER) 2007–2013 as well as by the Agence Nationale de la Recherche through the LABEX CEMPI project (ANR-11-LABX-0007).

Supplementary material

Supplementary material associated with this article can be found, in the online version, at 10.1016/j.cnsns.2015.11.025

References

[1] Glansdorff P, Prigogine I. Thermodynamic theory of structures. Stability and fluctuations. New York: Wiley; 1971.
[2] Nicolis G, Prigogine I. Self-organization in nonequilibrium systems. New York: J.Wiley & Sons; 1977.
[3] Pismen LM. Patterns and interfaces in dissipative dynamics. Springer series in Synergetics. Berlin Heidelberg: Springer; 2006.
[4] Cross M, Greenside H. Pattern formation and dynamics in nonequilibrium systems. New York: Cambridge University Press; 2009.
[5] Langer JS. Instabilities and pattern formation in crystal growth. Rev Mod Phys 1980;52:1.
[6] Fife PC. Dynamics of internal layers and diffusive interfaces. Philadelphia, Pennsylvania: Society for Industrial and Applied Mathematics; 1988.
[7] Collet P, Eckman JP. Instabilities and fronts in extended systems, Princeton series in physics. Princeton: Princeton University Press; 2014.
[8] Pomeau Y. Front motion, metastability and subcritical bifurcations in hydrodynamics. Physica D 1986;23:3.
[9] Eschenfelder AH. Magnetic bubble technology. Berlin Heidelberg: Springer; 1980.
[10] Clerc MG, Coulibaly S, Laroze D. Localized states beyond asymptotic parametrically driven amplitude equation. Int J Bifurc Chaos 2009;19:2717–26.
[11] Börzsönyi T, Akamatsu S, Faivre G. Weakly faceted cellular patterns versus growth-induced plastic deformation in thin-sample directional solidification of monoclinic biphenyl. Phys Rev E 2009;80:051601.
[12] Clerc MG, Residori S, Riera CS. First-order Fréedericksz transition in the presence of light-driven feedback in nematic liquid crystals. Phys Rev E 2001;63:060701; Clerc MG, Nagaya T, Petrossian A, Residori S, Riera C. First-order Fréedericksz transition and front propagation in a liquid crystal light valve with feedback. Eur Phys J D 2004;28:435; Residori S, Petrossian A, Nagaya T, Riera C, Clerc MG. Fronts and localized structures in a liquid-crystal-light-valve with optical feedback. Physica D 2004;199:149; Haudin F, Elías RG, Rojas RG, Bortolozzo U, Clerc MG, Residori S. Driven front propagation in 1D spatially periodic media. Phys Rev Lett 2009;103:128003; Rojas RG, Bortolozzo U, Clerc MG, Residori S. Front dynamics and pinning-depinning phenomenon in spatially periodic media. Phys Rev E 2010;81:056203.
[13] Petrov V, Ouyang Q, Swinney HL. Resonant pattern formation in a chemical system. Nature 1997;388:655.
[14] Douady S, Fauve S, Laroche C. Subharmonic instabilities and defects in a granular layer under vertical vibrations. Europhys Lett 1989;8:621; Melo F, Umbanhowar PB, Swinney HL. Hexagons, kinks, and disorder in oscillated granular layers. Phys Rev Lett 1995;75:3838; Moon SJ, Shattuck MD, Bizon C, Goldman DI, Swift JB, Swinney HL. Phase bubbles and spatiotemporal chaos in granular patterns. Phys Rev E 2001;65:011301; Macias JE, Clerc MG, Falcon C, Garcia-Nustes MA, Swift JB, Swinney HL. Spatially modulated kinks in shallow granular layers. Phys Rev E 2013;88:020201.

[15] van Saarloos W, Hohenberg H. Fronts, pulses, sources and sinks in generalized complex Ginzburg–Landau equations. Physica D 1992;56:303; Coullet P. Localized patterns and front nonequilibrium systems. Int J Bifurc Chaos 2002;12:2445–57.
[16] van Saarloos W. Front propagation into unstable states. Phys Rep 2003;386:29.
[17] Goldstein RE, Gunaratne GH, Gil L, Coullet P. Hydrodynamic and interfacial patterns with broken space-time symmetry. Phys Rev A 1991;43:6700.
[18] Andrade-Silva I, Clerc MG, Odent V. Asymmetric counterpropagating fronts without flow. Phys Rev E 2015;91:060501(R).
[19] Chomaz JM. Absolute and convective instabilities in nonlinear systems. Phys Rev Lett 1992;69:1931.
[20] Blanc C, Svensek D, Zumer S, Nobili M. Dynamics of nematic liquid crystal disclinations: The role of the backflow. Phys Rev Lett 2005;95:097802.
[21] Bogi A, Martinot-Lagarde P, Nobili M. Anchoring screening of defects interaction in a nematic liquid crystal. Phys Rev Lett 2002;89:225501.
[22] Dierking I, Ravnik M, Lark E, Healey J, Alexander G, Yeomans J. Anisotropy in the annihilation dynamics of umbilic defects in nematic liquid crystals. Phys Rev E 2012;85:021703.
[23] Oswald P, Pieranski P. Nematic and cholesteric liquid crystals. Boca Raton: Taylor and Francis group; 2005.
[24] Khoo IC. Liquid crystals. 2nd ed. New Jersey: John Wiley & sons; 2007.
[25] de Gennes PG, J P. The physics of liquid crystals. 2nd ed. Oxford: Clarendon Press; 1993.
[26] Chandrasekhar S. Liquid crystal. New York: Cambridge University Press; 1992.
[27] Andrade-Silva I, Clerc MG, Odent V. Zig-zag wall lattice in a nematic liquid crystal with an in-plane switching configuration. Phys Rev E 2014;90:022504.
[28] Shevchuk O, Reshetnyak V, Osyptchuk M. Director profile in the in-plane switching of nematic liquid crystals cell. Mol Cryst Liq Cryst 2004;422:1.
[29] Wang XY, Zhu ZS, Lu YK. Solitary wave solutions of the generalised Burgers–Huxley equation. J Phys A Math Gen 1990;23:271.
[30] Cessi P, Young WR. Fixed-flux convection in a tilted slot. J Fluid Mech 1992;237:57–71.
[31] Fredholm EI. Sur une classe d'équations fonctionnelles. Acta Math 1903;27:365.